JOURNAL OF PROPULSION AND POWER
Vol. 21, No. 1, January–February 2005

Numerical Analysis for Propellant Management in Rocket Tanks

Takehiro Himeno* and Toshinori Watanabe†
University of Tokyo, Tokyo 113-8656, Japan
and
Akira Konno‡
Japan Aerospace Exploration Agency, Ibaraki 305-8505, Japan

To track the three-dimensional behavior of liquid surfaces in storage tanks on orbit, a numerical scheme based on the level set method was developed. For the verification of the numerical methods, experimental data were acquired through the observation of the unsteady deformations of liquid surfaces in cylindrical containers under low-gravity conditions in a drop tower. Primary emphasis was placed on the dynamic behavior of the liquid surface and the displacement of the contact line on the solid wall. Based on the results, the boundary condition for surface tension was discussed and the model of wetting phenomena was adequately introduced into the computation. Compared with the experimental data, the corresponding numerical results showed good agreement. With the developed code, the flowfields at the draining process in the liquid oxygen (LO_X) tank for the upper-stage propulsion system of an H-IIA launch vehicle under low-gravity conditions were also investigated. It was found that the buoyancy induced by a slight acceleration was efficient to prevent dip growth and that the serviceable propellant in the launch-vehicle tank could thereby be increased in a realistic situation.

Nomenclature

C_p, C_v	=	specific heat at constant p or T, J/(kg · K)
C_S	=	sound velocity, m/s
Ca	=	Capirally number, $\mu U/\sigma$
D	=	diameter of cylinder, m
e	=	internal energy, J/kg
$\boldsymbol{g}$	=	gravity acceleration, m/s^2
H_ε	=	approximate Heaviside function
h_{init}	=	initial height of interface, m
J	=	Jacobian
k	=	thermal conductivity, W/(m^2 · K)
p	=	static pressure, Pa
$\dot{Q}$	=	flow rate of draining, m^3/s
$\boldsymbol{q}$	=	heat flux, W/m^2
T	=	temperature, K
t	=	time, s
t_S	=	time of vapor suction, s
$\boldsymbol{u}$	=	velocity, m/s
We	=	Weber number, $\rho U^2 D/\sigma$
Z_{CP}	=	displacement of contact line, m
γ	=	ratio of specific heat, C_p/C_v
δ_ε	=	approximate delta function, 1/m
ε	=	thickness of interface in computation, m
ζ_{CP}	=	Z_{CP} normalized by D, Z_{CP}/D
θ_E, θ_A, θ_R	=	equilibrium, advancing, or receding contact angle
μ, λ	=	first or second viscosity coefficient, Pa · s
μ_J	=	Joule–Thomson coefficient, K/Pa
ξ, η, ζ	=	generalized coordinates in computation, m
ρ	=	density, kg/m^3
σ	=	surface tension, N/m
τ	=	scaled time, $t/[D^3/(\sigma/\rho)]^{1/2}$
ϕ	=	distance function from interface, m
φ	=	initial inclination of interface
∇	=	nabla operator, 1/m

Presented as Paper 2001-3822 at the 37th AIAA/ASME/SAE/ASEE Joint Propulsion Conference and Exhibit, Salt Lake City, UT, 8 July 2001; received 26 August 2003; revision received 8 March 2004; accepted for publication 21 March 2004.

*Lecturer, Department of Aeronautics and Astronautics, 7-3-1 Hongo, Bunkyo-ku. Member AIAA.

†Associate Professor, Department of Aeronautics and Astronautics, 7-3-1 Hongo, Bunkyo-ku. Member AIAA.

‡Deputy Project Manager, H-IIA Project Team, Office of Space Flight and Operations, 2-2-1 Sengen, Tsukuba-shi. Member AIAA.

Introduction

WITH the progress of human activities in space, the handling of liquids under low-gravity conditions is becoming more frequent. In weightless flights, the absence or diminution of the gravity force makes it extremely difficult to position and control a two-phase fluid in a desirable manner.[1,2]

For the establishment of the technology for fluid management in space, it is essential to accumulate technical knowledge to give an appropriate assessment of designed fluid management systems for space application. However, there are not so many opportunities to realize the low-gravity state with airplanes or drop towers. Investigation methods using computational fluid dynamics (CFD) are therefore strongly desired.

In the present paper, the cubic-interpolated propagation level set method (CIP-LSM)[3,4] algorithm was developed to simulate the three-dimensional behavior of liquid flow driven by surface tension, wetting phenomena, and gravity force. The free-surface flows under low-gravity conditions were both experimentally and numerically investigated to verify the algorithm and to study the appropriate boundary conditions.

Drop-Tower Experiment

In the present study, the unsteady deformations of liquid surfaces under low-gravity conditions were observed through a transparent vessel of cylindrical shape. The series of experiments were aimed at acquiring the basic knowledge of free-surface flows driven by surface tension and at obtaining data suitable for the verification of the CFD code and the discussion of the boundary condition.

Experimental Facilities

The present experiments were conducted at the drop tower, shown in Fig. 1, constructed at the University of Tokyo. As shown in Fig. 2, the drop box was composed of an inner box, including the test vessel made of polyacrylate resin, and an outer box 920 mm wide, 610 mm deep, and 700 mm high. The liquid behavior was observed through transparent walls of the test vessel with the charge-coupled

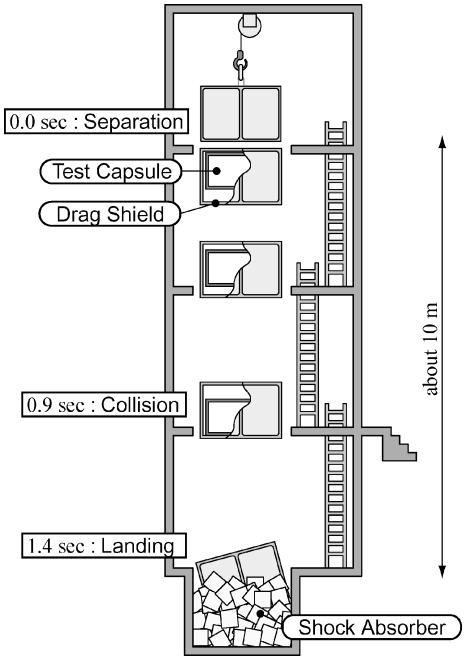

Fig. 1 Schematic configuration of the drop tower.

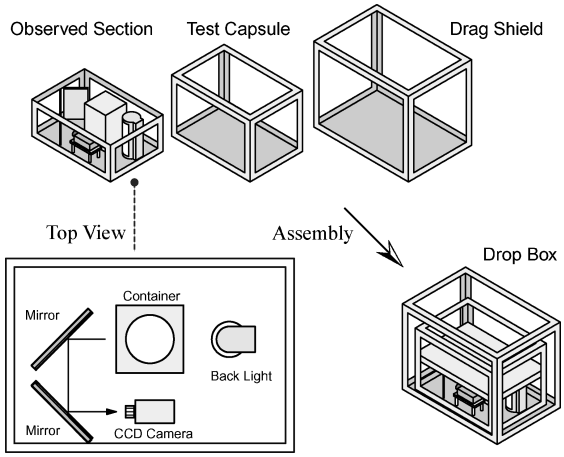

Fig. 2 Schematic configuration of the drop box.

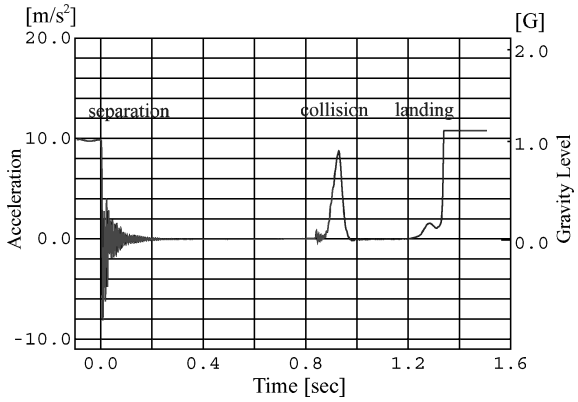

Fig. 3 History of gravity level, measured.

device camera equipped on the observation section and recorded on a videocassette recorder.

Figure 3 shows time variation of vertical acceleration during the dropping, measured with the accelerometer attached on the observation section. The steady low-gravity condition obtained in the present experiment is about $10^{-3}g$ with the duration of 0.9 s. The detected oscillation following the separation was the natural vibration of the drop box caused by the release of the gravitational load. Because the amplitude of displacement was estimated below 0.1 mm, this vibration was judged not to affect the observed flowfields.

The outer box acted as a drag shield and decelerated by the aerodynamic force. The inner box thus caught up the outer one at 0.9 s after the separation when an impact as large as about $1g$ was detected. The drop box landed with a large acceleration after about a 1.4-s drop.

Table 1 Physical properties of the tested liquids

Liquid	ρ, kg/m^3	σ, 10^{-3} N/m	σ/ρ, 10^{-6} m^3/s^2	μ, 10^{-3} Pas	θ_E, deg
Ethanol	790	22.80	28.9	1.08	0
FC-77	1780	15	8.4	1.42	0
Ethyl benzene	867	29.84	34.4	——	0
Ethyl laurate	867	28.76	33.2	——	0
Ethylene glycol	1113	47.99	43.1	——	20
Water	998	72.75	72.9	1.00	80

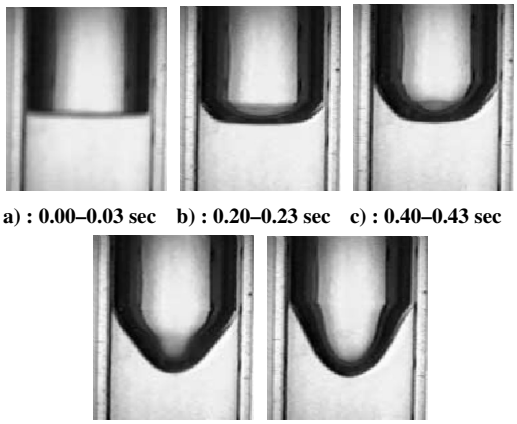

a) : 0.00–0.03 sec b) : 0.20–0.23 sec c) : 0.40–0.43 sec

d) : 0.60–0.63 sec e) : 0.80–0.83 sec

Fig. 4 Observed deformation of liquid surface in a cylindrical vessel (ethanol and polyacrylate resin, $D = 80$ mm).

Operating Fluids

In general, the propagation velocity of a capillary wave on a liquid surface is in proportion to the value of the parameter $(\sigma/\rho)^{1/2}$, where σ and ρ denote the surface tension coefficient of the interface and the density of the liquid, respectively. In wetting phenomena, the advancing rate of the contact line increases with increase in $\cos(\theta_E)$. The liquid with larger values of both $(\sigma/\rho)^{1/2}$ and $\cos(\theta_E)$ could be expected to perform large and quick surface deformation.

In this paper, ethanol (C_2H_5OH) and perfluorocarbon (C_8F_{18}: FC-77) were chosen as operating fluids. The physical properties of these liquids are collected in Table 1, where θ_E denotes equilibrium contact angle of each liquid on the plate made of polyacrylate resin. The additional results with other liquids such as ethyl benzene, ethyl laurate, and ethylene glycol are shown in Ref. 5.

Results and Discussions

Figure 4 shows the observed deformation of ethanol surface with time. The diameter of the cylindrical vessel, D, was set to be 80 mm and its height was 260 mm. Before the dropping, even under normal gravity condition, there was a small meniscus at the wall. The height of this meniscus scaled with the capillary length $l_C = \{(\sigma/\rho)/g\}^{1/2}$, which was about 1.7 mm in the present case. After the release of the drop box, during the low-gravity state before the collision, it was observed that the contact line advanced toward the vapor side and the deformation propagated on the interface toward the vessel center as capillary waves. In the initial period of dropping, the liquid pressure near the small meniscus became unbalanced with the vapor pressure and caused the initial rise of the contact line. After this inertia-driven time domain, the wetting forces took over and the flow became capillary dominated. In Refs. 6 and 7, an intensive

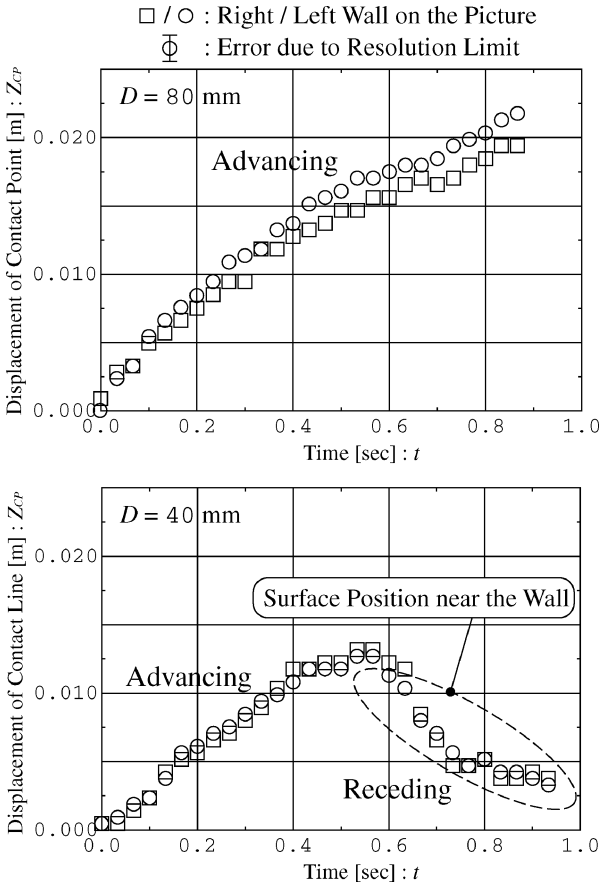

Fig. 5 Level of contact line as a function of time ($D = 80$ and 40 mm).

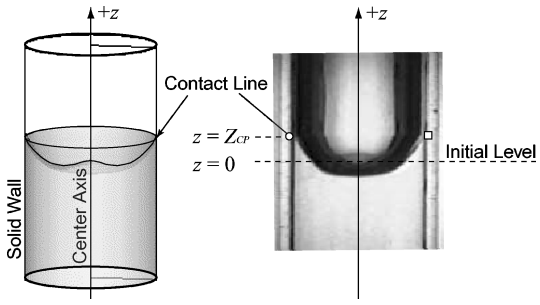

Fig. 6 Specification of contact level.

investigation is presented on the behavior of contact line and the reorientation phenomena of liquid surfaces after the step reduction of gravity with a drop tower.

Figure 5 shows the displacement of the contact line, denoted by Z_{CP}, as a function of the time elapsed from the start of dropping. As shown in Fig. 6, the position of the contact line was specified by the pixel on the image recorded on videotape. In the present observation, due to the poor resolution of video images, the error of Z_{CP} was estimated as about 2 mm, the flame rate of which was about 1/30 s. The origin of the coordinate system in the picture was determined as the section of the center axis and the initial level of contact line.

In the case with $D = 80$ mm, as shown in Fig. 5, it was observed that the accelerated contact line was gradually decelerating. The period of the low-gravity environment came to an end, due to the collision, before the contact line decelerated to rest at the maximum height. In the other case, with $D = 40$ mm, the capillary wave went to the center and came back to the wall under the continuation of a low-gravity state. It was also seen that the contact line advanced to the maximum height and receded to the liquid side.

It was reported,[6,7] however, that for the perfect wetting liquid, such as ones used in this experiment, the contact line does not recede

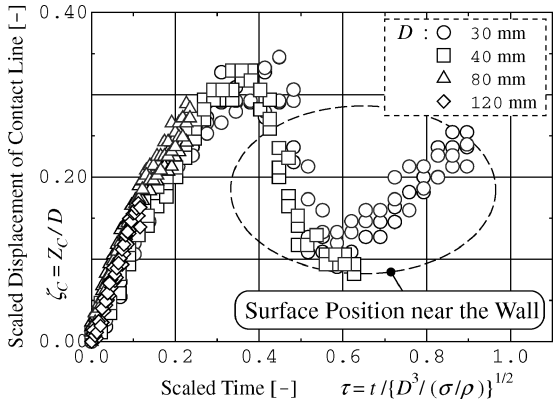

Fig. 7 Similarity rule: $\zeta_{CP} = \zeta_{CP}(\tau, \theta)$; ethanol; $D = 30$, 40, 80, and 120 mm.

after attaining the maximum height and the thin layer of liquid remains on the wall. Because of the poor resolution of the video images, the surface position near the wall was thought to be detected as Z_{CP}. Hence, note that the receding data points in Fig. 5 do not represent the position of the contact line itself.

The experiments were conducted on cylinders of various diameters ranging from 30 to 150 mm. In Fig. 7, the changes of the scaled displacement of the contact line, $\zeta_{CP} = Z_{CP}/D$, were plotted as a function of the scaled time $\tau = t/t_{ro}$, where $t_{ro} = \{D^3/(\sigma/\rho)\}^{1/2}$ denotes the reorientation time, defined as the period taken for the capillary wave with the wavelength of D to propagate for a distance equal to a diameter D. Though the diameter D was varied as 30, 40, 80 and 120 mm, the scaled displacement ζ_{CP} has good correlation with the scaled time τ, especially during the advancing period before reaching the maximum height. Hence, as long as D is larger than 30 mm, the similarity law in terms of Weber number, $We = \rho U^2 D/\sigma$, was established and the viscosity of ethanol was not dominant in the flowfield.

If the viscosity is negligible—in other words, if the value of the Capirally number, $Ca = (\mu U/\sigma)$, in terms of the advancing speed is small enough, where U scales $[(\sigma/\rho)/D]^{1/2}$ and decreases as τ increases—the dynamic contact angle closes with the static advancing contact angle θ_A, which is a constant angle independent of the cylinder diameter. Indeed, judging from the obtained images, the inclination of the liquid surface near the cylinder wall was seen to be kept almost constant at about 30 to 35 deg. But the value of the dynamic contact angle itself could not be measured due to the resolution limit.

Numerical Method

In the present study, a numerical method, called CIP-LSM,[3,4] was developed to simulate three-dimensional changes of the free-surface shape affected by surface tension, wetting phenomena, and gravity force. In this method, the CIP combined unified procedure (CCUP)[8] scheme is coupled with LSM[9,10] and continuum surface force CSF[11] model. By the application of the CIP[12,13] scheme not only to advection but also to the reinitialization of the level set function, the shape of the gas–liquid interface is distinctly tracked on the fixed-grid system, and the surface tension is estimated as a body force.

Governing Equations

In this method, no-slip velocity between gas phase and liquid phase is assumed. Both gas and liquid flows are described by Navier–Stokes equations for homogeneous two-phase flow as follows:

$$\frac{\partial \rho}{\partial t} + (\boldsymbol{u} \cdot \nabla)\rho = -\rho \nabla \cdot \boldsymbol{u} \tag{1}$$

$$\rho \frac{\partial \boldsymbol{u}}{\partial t} + \rho(\boldsymbol{u} \cdot \nabla)\boldsymbol{u} = \nabla : \boldsymbol{\Pi} + \boldsymbol{g} \tag{2}$$

$$\rho \frac{\partial e}{\partial t} + \rho(\boldsymbol{u} \cdot \nabla)e = \{\boldsymbol{\Pi} : \nabla\} \cdot \boldsymbol{u} - \nabla \cdot \boldsymbol{q} \tag{3}$$

where ρ, $\boldsymbol{u}$, and e denote density, velocity, and energy, respectively, and the vectors $\boldsymbol{g}$ and $\boldsymbol{q}$ appearing in the right-hand sides denote gravity and heat flux. The stress tensor $\boldsymbol{\Pi}$ includes the tensors of pressure $p\boldsymbol{I}$, surface tension $\boldsymbol{T}_\sigma$, and viscous force $\boldsymbol{T}_v$. With the unit vector perpendicular to the gas–liquid interface denoted by $\boldsymbol{n}_s$ and the deformation tensor $\boldsymbol{D}$ defined as $\nabla\boldsymbol{u}$, each tensor is written as follows:

$$\boldsymbol{\Pi} = -p\boldsymbol{I} + \boldsymbol{T}_\sigma + \boldsymbol{T}_v \tag{4}$$

$$\boldsymbol{T}_\sigma = \sigma\delta_S(\boldsymbol{I} - \boldsymbol{n}_S\boldsymbol{n}_S) \tag{5}$$

$$\boldsymbol{T}_v = \lambda(\nabla\cdot\boldsymbol{u})\boldsymbol{I} + \mu(\boldsymbol{D} + \boldsymbol{D}^T) \tag{6}$$

where σ, λ, and μ represent the coefficients of surface tension, and first and second viscosity, respectively.

To specify the fluid phase at a certain point in the flowfield, the level set function ϕ is introduced, which has as much value as the signed distance from the gas–liquid interface. Furthermore, the Heaviside function H_S is defined as follows:

$$\begin{aligned} H_S &= 0.5 \quad \text{if} \quad \phi > 0 : \text{liquid} \\ H_S &= 0 \quad \text{if} \quad \phi = 0 : \text{interface} \\ H_S &= -0.5 \quad \text{if} \quad \phi < 0 : \text{gas} \end{aligned} \tag{7}$$

Then, the delta function δ_S in Eq. (5) is expressed as

$$\nabla H_S = \delta_S\boldsymbol{n}_S \tag{8}$$

and the physical properties such as density or viscosity at the point are switched by Eq. (9):

$$\rho = 0.5(\rho_{\text{Liq}} + \rho_{\text{Gas}}) + H_S(\rho_{\text{Liq}} - \rho_{\text{Gas}}) \tag{9}$$

The properties with the subscript of Liq or Gas represent the values for the liquid phase or gas phase. They are calculated with the equation of state or the other empirical formula described by pressure p and temperature T at that point; that is,

$$\rho_{\text{Liq}} = \rho_{\text{Liq}}(p, T) \tag{10}$$

$$\rho_{\text{Gas}} = \rho_{\text{Gas}}(p, T) \tag{11}$$

In the present study, because the phase change is not assumed and each fluid particle keeps its initial phase attribution, the level set function is also advected according to

$$\frac{\partial\phi}{\partial t} + (\boldsymbol{u}\cdot\nabla)\phi = 0 \tag{12}$$

Thus, the position of interface is implicitly expressed as zero level set and is tracked indirectly.

Thermo-Cubic-Interpolated Propagation Combined Unified Procedure Scheme

The basic equations (1–3) are solved with the CCUP[8] scheme proposed by Yabe et al. Figure 8 shows the algorithm of CCUP schematically, where the change of the flowfield in a computational time step Δt is divided into an advection phase and a nonadvection phase.

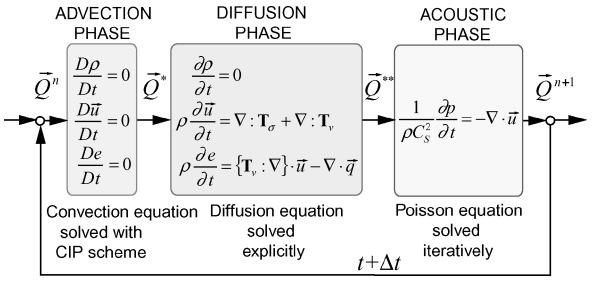

Fig. 8 Algorithm of CCUP scheme.

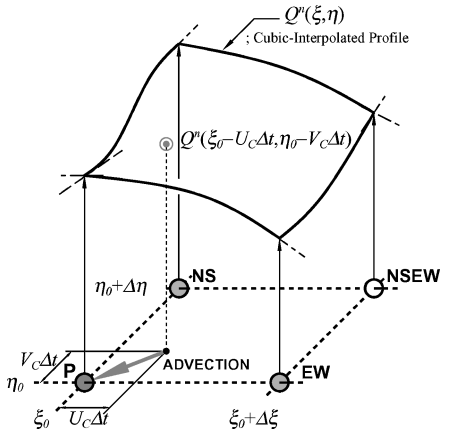

Fig. 9 Convection equation solved with CIP scheme.

phase. The nonadvection phase is again divided into a diffusion phase and an acoustic phase.

Whereas the combination of independent variables in the original CCUP was selected as $\boldsymbol{Q} = (\boldsymbol{u}, \rho, p)^T$, the combination in this paper was changed to $\boldsymbol{Q} = (\boldsymbol{u}, T, p)^T$ and the algorithm was modified. By solving temperature T directly, the heat transfer even in the incompressible flowfield can be adequately simulated. Therefore, the present method was named thermo-CCUP TCUP.[5]

In the advection phase, the convection equations (12) and (13) are solved with the CIP scheme[12,13]:

$$\frac{\partial\boldsymbol{Q}}{\partial t} + (\boldsymbol{u}\cdot\nabla)\boldsymbol{Q} = 0 \tag{13}$$

For instance, suppose that the convection equation

$$\frac{\partial Q}{\partial t} + U_C\frac{\partial Q}{\partial\xi} + V_C\frac{\partial Q}{\partial\eta} = 0 \tag{14}$$

is solved with the CIP scheme on a generalized coordinate system in a two-dimensional domain, where the contravariant velocities denoted by U_C and V_C are defined as $\boldsymbol{u}\cdot\nabla\xi$ and $\boldsymbol{u}\cdot\nabla\eta$, respectively. As shown in Fig. 9, the profile of the variable Q is interpolated with cubic polynomial as follows:

$$\begin{aligned} Q^n(\xi,\eta) &= C_{30}\xi^3 + C_{21}\xi^2\eta + C_{12}\xi\eta^2 + C_{03}d\eta^3 \\ &\quad + C_{20}\xi^2 + C_{11}\xi\eta + C_{02}\eta^2 + C_{10}\xi + C_{01}\eta + C_{00} \end{aligned} \tag{15}$$

The coefficients C_{ij} are determined by the values Q and gradients Q_ξ and Q_η of the variant at neighboring grid points in the upwind direction. Then, according to the theoretical solution, the cubic-interpolated profile is shifted and the value at (ξ_0, η_0) is calculated by,

$$Q^*(\xi_0,\eta_0) = Q^n(\xi_0 - U_c\Delta t, \eta_0 - V_C\Delta t) \tag{16}$$

where the superscript * represents the quantities obtained after the operation of the advection phase. The same algorithm applies to the three-dimensional problems.[14]

In the diffusion phase, the changes of variables $\boldsymbol{Q}$ caused by the dispersion of momentum and heat were solved. Because the density ρ remains unchanged in this phase, the variations in pressure and temperature are calculated by,

$$\frac{T^{**} - T^*}{\Delta t} = \frac{\gamma^*}{(\rho C_p)^*}\tilde{Q}_{\text{DIF}} \tag{17}$$

$$\frac{p^{**} - p^*}{\Delta t} = \frac{\gamma^* - 1}{(1 + \rho C_p\mu_J)^*}\tilde{Q}_{\text{DIF}} \tag{18}$$

where C_p, γ, and μ_J are specific heat at constant pressure, ratio of specific heat, and Joule–Thomson coefficient, respectively, and the

superscript ** denotes the quantities after the diffusion phase. Heat input denoted by $\tilde{Q}_{\mathrm{DIF}}$ is calculated as follows:

$$\tilde{Q}_{\mathrm{DIF}} = \nabla \cdot [\boldsymbol{T}_v : \boldsymbol{u} - \boldsymbol{q}]^* - \frac{\rho^*}{2}\frac{\partial \boldsymbol{u}^2}{\partial t} \tag{19}$$

In the acoustic phase, on the assumption of isentropic change, the acoustic equation described as

$$\frac{1}{\rho C_S^2}\frac{\partial p}{\partial t} = -\nabla \cdot \boldsymbol{u} \tag{20}$$

is discretized in the timewise direction into

$$\frac{1}{\left(\rho C_S^2\right)^{**}}\frac{p^{n+1} - p^{**}}{\Delta t} = -\nabla \cdot \boldsymbol{u}^{**} + \nabla\left(\frac{\nabla p^{n+1}}{\rho^{**}}\right)\Delta t \tag{21}$$

where C_S represents sound velocity, and is solved implicitly via the stabilized bi-conjugate gradient, BiCGSTAB method. The accompanying change of temperature is calculated by

$$T^{n+1} - T^{**} = \frac{(1 + \rho C_p \mu_J)^{**}}{(\rho C_p)^{**}}(p^{n+1} - p^{**}) \tag{22}$$

In Table 2, the TCUP algorithm is summarized. The physical properties concerning compressibility required in this procedure can be calculated by the following formulas coupled with the equation of state:

$$C_p(T, p) = C_p(T, p_0) - \int_{p_0}^{p} T\left[\frac{\partial^2}{\partial T^2}\left(\frac{1}{\rho}\right)\right]_p \mathrm{d}p \tag{23}$$

$$C_v(T, p) = C_p(T, p) - T\left(\frac{\partial p}{\partial T}\right)_\rho \left[\frac{\partial}{\partial T}\left(\frac{1}{\rho}\right)\right]_p \tag{24}$$

$$\gamma(T, p) = \frac{C_p(T, p)}{C_v(T, p)} \tag{25}$$

$$C_S^2(T, p) = \gamma(T, p)\left(\frac{\partial p}{\partial \rho}\right)_T \tag{26}$$

Table 2 Algorithm of TCUP

Variant	$: \boldsymbol{Q} = (\boldsymbol{u},\ p,\ T)^T$
Advection Phase	$: \boldsymbol{Q}^n$ to $\boldsymbol{Q}^*$
$\boldsymbol{Q}$	$\frac{\partial \boldsymbol{Q}}{\partial t} + U_C\frac{\partial \boldsymbol{Q}}{\partial \xi} + V_C\frac{\partial \boldsymbol{Q}}{\partial \eta} + W_C\frac{\partial \boldsymbol{Q}}{\partial \zeta} = \boldsymbol{0}$
	: solved with CIP scheme.
Diffusion Phase	$:\boldsymbol{Q}^*$ to $\boldsymbol{Q}^{**}$
$\boldsymbol{u}$	$\int_\Omega \rho^*\frac{\boldsymbol{u}^{**} - \boldsymbol{u}^*}{\Delta t}\mathrm{d}V = \int_\Omega \nabla : \boldsymbol{T}_v^*\,\mathrm{d}V = \int_{\partial\Omega} \boldsymbol{T}_v^* : \mathrm{d}\boldsymbol{S}$
T	$\frac{T^{**} - T^*}{\Delta t} = \frac{\gamma^*}{(\rho C_p)^*}\tilde{Q}_{\mathrm{DIF}}$
p	$\frac{p^{**} - p^*}{\Delta t} = \frac{\gamma^* - 1}{(1 + \rho C_p \mu_J)^*}\tilde{Q}_{\mathrm{DIF}}$
	: solved explicitly.
Acoustic Phase	$:\boldsymbol{Q}^{**}$ to $\boldsymbol{Q}^{n+1}$
p	$\int_\Omega \frac{p^{n+1} - p^{**}}{\left(\rho C_S^2\right)^{**}\Delta t}\mathrm{d}V = -\int_{\partial\Omega}\left(\boldsymbol{u}^{**} - \frac{\nabla p^{n+1}}{\rho^{**}}\Delta t\right)\cdot \mathrm{d}\boldsymbol{S}$
	:solved with iterative method (BiCG-STAB).
$\boldsymbol{u}$	$\frac{\boldsymbol{u}^{n+1} - \boldsymbol{u}^{**}}{\Delta t} = -\frac{\nabla p^{n+1}}{\rho^{**}}$
T	$T^{n+1} - T^{**} = \frac{(1 + \rho C_p \mu_J)^{**}}{(\rho C_p)^{**}}(p^{n+1} - p^{**})$
	:solved explicitly.

$$\mu_J(T, p) = -\frac{1}{\rho C_p}\left[T\frac{1}{\rho}\left(\frac{\partial \rho}{\partial T}\right)_p + 1\right] \tag{27}$$

Neither the assumption of incompressibility nor a particular equation of state is prescribed. TCUP can, therefore, simulate the flowfields, including various kinds of fluids in liquid or gaseous state together.

Level Set Method

With the aid of the LSM[9] proposed by Sussman et al., the gas–liquid interface was tracked on the fixed-grid system. In this method, the Heaviside function H_S, defined as Eq. (7), is modified to the following H_ε using the level set function ϕ, which represents a signed distance from the gas–liquid interface:

$$H_\varepsilon = 0.5 \cdot \max\{-1.0, \min[1.0, \phi/\varepsilon + 1/\pi \sin(\pi\phi/\varepsilon)]\} \tag{28}$$

In Fig. 10, the translation between the extended function H_ε and the level set function ϕ is shown by the solid curve. The physical properties at an arbitrary grid point are expressed by

$$\rho = 0.5(\rho_{\mathrm{Liq}} + \rho_{\mathrm{Gas}}) + H_\varepsilon(\rho_{\mathrm{Liq}} - \rho_{\mathrm{Gas}}) \tag{29}$$

Hence, the gas–liquid interface was captured as a transition zone with a thickness of 2ε. For example, when these functions, H_ε and ϕ, are defined in the flowfield of Fig. 6, their contour lines are drawn as shown in Fig. 11.

As shown in Fig. 12, the level set function has the property of a distance function and the unit vector $\boldsymbol{n}_S$ perpendicular to its contours, and the curvature κ of the lines can be calculated as follows:

$$\boldsymbol{n}_S = \frac{\nabla\phi}{|\nabla\phi|} \tag{30}$$

$$\kappa = \nabla \cdot \boldsymbol{n}_S = \nabla \cdot \left(\frac{\nabla\phi}{|\nabla\phi|}\right) \tag{31}$$

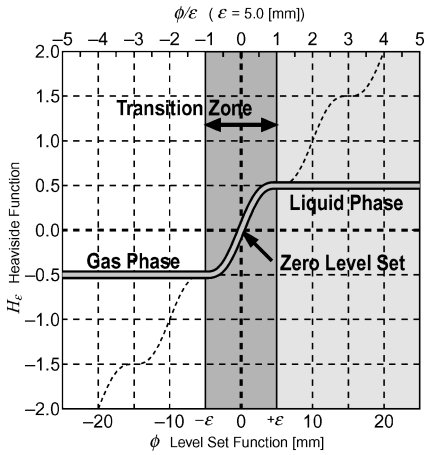

Fig. 10 Translation between H_ε and ϕ.

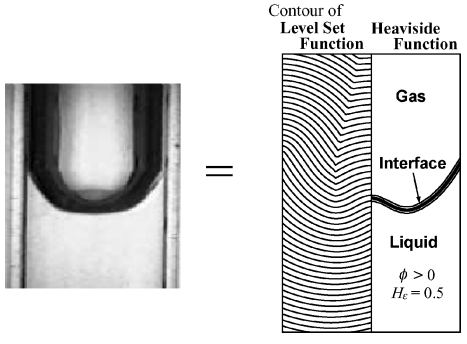

Fig. 11 H_ε and ϕ defined in the flowfield of Fig. 6.

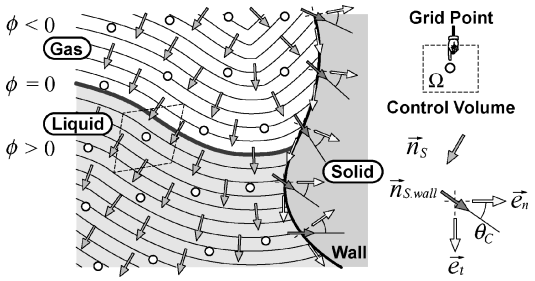

Fig. 12 Normal vector n_S and curvature κ of interface calculated from the distribution of ϕ.

Then, with the CSF model[11] proposed by Brackbill et al. and by the approximated delta function δ_ε, defined as

$$\delta_\varepsilon = \frac{\partial H_\varepsilon}{\partial \phi} \tag{32}$$

the surface force appearing in the right-hand side of Eq. (2) can be described as follows:

$$\boldsymbol{F}_{S\cdot\perp} = \nabla : \boldsymbol{T}_\sigma = \nabla : \{\sigma\delta_S(\boldsymbol{I} - \boldsymbol{n}_S\boldsymbol{n}_S)\}$$
$$= -\sigma\kappa\boldsymbol{n}_S\delta_S = -\sigma\kappa\boldsymbol{n}_S\delta_\varepsilon = -\sigma[\nabla\cdot(\nabla\phi/|\nabla\phi|)](\nabla H_\varepsilon/|\nabla\phi|) \tag{33}$$

where, surface tension σ is supposed to be constant.

In the analysis by the LSM, the most important issue for the level set function is to remain the property of distance function, which can be described by

$$|\nabla\phi| = 1, \tag{34}$$

because the information on the surface configuration is obtained from the spatial distribution of the level set function. To keep this property against the disturbance caused by the advection, an operation called reinitialization was proposed by Sussman et al. In the process, the following equation is iteratively solved at every time step:

$$\frac{\partial\phi}{\partial\tilde{t}} = S_{\mathrm{LSM}}(1 - |\nabla\phi|) \tag{35}$$

$$S_{\mathrm{LSM}} = \frac{\phi}{\sqrt{\phi^2 + (\varepsilon/2)^2}} \tag{36}$$

where $\tilde{t}$ represents virtual time for the iteration.

In the present study, Eq. (35) was transformed into convection equation (37):

$$\frac{\partial\phi}{\partial\tilde{t}} + \boldsymbol{w}_{\mathrm{LSM}}\cdot\nabla\phi = S_{\mathrm{LSM}} \tag{37}$$

where

$$\boldsymbol{w}_{\mathrm{LSM}} = S_{\mathrm{LSM}}\boldsymbol{n}_S \tag{38}$$

and the left-hand side of Eq. (37) was solved by means of the CIP scheme.[12,13] Owing to the application of the CIP scheme not only to the advection but also to the reinitialization of the level set function, the shape of the interface can be distinctly captured on the fixed-grid system.

In the improved version of the CIP-LSM,[14] the volume fraction is introduced as an independent variable and the surface movement is traced by Multi-Interface Advection and Reconstruction Solver, (MARS)[15,16] and then the level set function is produced by the CIP for the calculation of curvature. MARS is a kind of VOF,[17] volume-of-fluid algorithm like PLIC,[18] Piecewise Linear Interface Calculation.

Contact-Angle Model

To simulate the wetting phenomena on a solid wall, the contact angle θ was introduced. In Fig. 12, the unit vector perpendicular to the wall is $\boldsymbol{e}_n$ and the unit vector tangential to the wall is $\boldsymbol{e}_t$. Both vectors are also perpendicular to the contact line. Then, as the boundary condition on the solid wall, the vector $\boldsymbol{n}_S$ was fixed to be

$$\boldsymbol{n}_{S\cdot\mathrm{wall}} = \boldsymbol{e}_n\cos(\theta) + \boldsymbol{e}_t\sin(\theta) \tag{39}$$

When the configuration of the wall is given as the contour surface of a generalized coordinate ξ, for instance, the vectors are calculated with the value of metrics as follows:

$$\boldsymbol{e}_n = \nabla\xi/|\nabla\xi| \tag{40}$$

$$\boldsymbol{e}_t = [\nabla\phi - (\boldsymbol{e}_n\cdot\nabla\phi)\boldsymbol{e}_n]/|\nabla\phi - (\boldsymbol{e}_n\cdot\nabla\phi)\boldsymbol{e}_n| \tag{41}$$

There still remains the problem of how to determine the value of the contact angle.

Several models[6] of the dynamic contact angle were proposed as a function of θ_A, θ_R, and Ca. In this model, because the viscous effect on the behavior of the contact line is merged into θ, the slip condition for the velocity is usually imposed on the solid wall. The static advancing and receding contact angles, θ_A and θ_R, are determined from experiments. The general form of the "slip-type" models including the hysteresis of wetting is written as

$$\theta = f(\theta_A, \theta_R, Ca) \tag{42}$$

In the case of small Ca, it can be simplified as

$$\theta = 0.5[(\theta_A + \theta_R) + (\theta_A - \theta_R)\ \mathrm{sgn}(u_{\mathrm{BL}})] \tag{43}$$

where u_{BL} denotes the advancing speed of the contact line, which is estimated in terms of the velocity near the wall as follows:

$$u_{\mathrm{BL}} = -\boldsymbol{e}_t\cdot\boldsymbol{u} \tag{44}$$

On the other hand, an alternative idea is the model coupled with a nonslip condition. In such models, the effect of viscosity is distinguished from that of surface tension and the viscous stress on the wall acts directly on the fluid momentum. If the governing equations are discretized on the basis of the finite volume method and, as shown in Fig. 12, if the grid point is not allocated on the wall, the nonslip condition and the advancing of the contact line do not conflict in the computation. The simplest form of the "non-slip-type" models is thought to be

$$\theta = \theta_E \tag{45}$$

The parameter is utilized just for the calculation of the surface force and does not constrain the geometric configuration of the surface near the wall.

Verification of the Method

To verify the accuracy of the developed code, the flowfields in the cylinder observed with the drop tower were simulated. The primary emphasis was placed on whether the CIP-LSM could capture the important features of the surface deformation, such as the rising liquid along the wall and the capillary wave reflected at the center. The dynamic behavior of the contact line was also compared between the experimental data and the numerical results. The test parameters in the simulated cases are collected in Table 3.

Table 3 Test parameters

ID	Case 1	Case 2	Case 3
Operating fluid	Ethanol	Ethanol	FC-77
Contact angle	$\theta_E = 0$	$\theta_E = 0$	$(\theta_A, \theta_R) = (20, 0)$
Shape of container	Cylinder	Cylinder	Rectangular
(Dimension)	($D = 80$)	($D = 150$)	($L = 250$)
2ε, mm	3	6	6
Gravity	zero	With impact	With impact

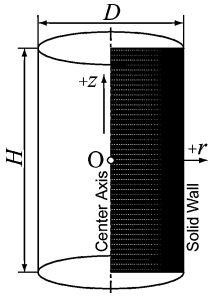

Fig. 13 Grid system for case 1 (59 × 180 grid points, $D = 80$ mm, $H = 120$ mm).

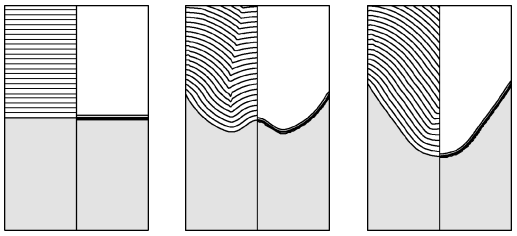

a) : 0.00 sec **b) : 0.40 sec** **c) : 0.80 sec**

Fig. 14 Deformation of liquid surface in a cylindrical vessel, computation: (ethanol and polyacrylate resin, $D = 80$ mm).

Axisymmetric Deformation

In cases 1 and 2, ethanol and air were utilized as the combination of operating fluids. Both liquid and gas phases were assumed to be incompressible, and other physical properties were given as the values at the temperature of 298 K.

Figure 13 shows the computational domain for case 1. Corresponding to the experiment, the diameter of the cylindrical vessel, D, was 80 mm. On the other hand, the height was limited to 120 mm, which was thought to be long enough to neglect the influence of the top and bottom walls. With the assumption that the flowfield was axisymmetric, the basic equations were solved on only one meridian section and 59×180 grid points were arranged in the r and z directions. At the initial condition, the zero level set ($\phi = 0$) was given as a flat plane located on the middle level, and the thickness of the interface 2ε was given to be 3 mm. In these cases, the small meniscus near the wall was neglected, but it cannot be negligible when D is comparable to the capillary length l_C. The gravity acceleration acting on the domain was zero during the computation. For the contact angle, the non-slip-type model described by Eq. (45) was utilized and the parameter θ_E was set to be 0 deg in cases 1 and 2.

Figure 14 shows the numerical results of case 1. The shape of the interface at each time is indicated by the contours of the Heaviside function H_ε drawn in the right-hand side of each panel, while the contour of the level set function ϕ is shown on the left-hand side. Compared with the corresponding data shown in Figs. 4 and 7, it can be judged that quite good agreement is obtained between the computation and the experiment.

Figure 15 shows the scaled displacement of contact lines obtained in the computation by a solid line, where the experimental data are plotted together. The computed contact line Z_{CP} was detected as the position at $\phi = 0$ on the boundary. In the CIP-LSM, as described by Eq. (2), the dynamic deformation of the local surface was determined by the balance among the surface force, the viscous force, and the inertia of the fluid. Because the advancing speed of the contact line was also determined as a result of the balance, the surface near the wall was thought to show a similar contact angle and advancing behavior to those in the experiment, despite θ_E being set to be zero.

The calculation was continued for a longer period than for that in the experiment. Once the contact line reached the maximum height, a receding and oscillating contact line was observed. But, as mentioned earlier, it was possible that the very thin layer of liquid should have remained on the wall and the contact line should have been pinned at the maximum position. Since the grid size near the wall was 0.2 mm, the present computation might not capture the layer.

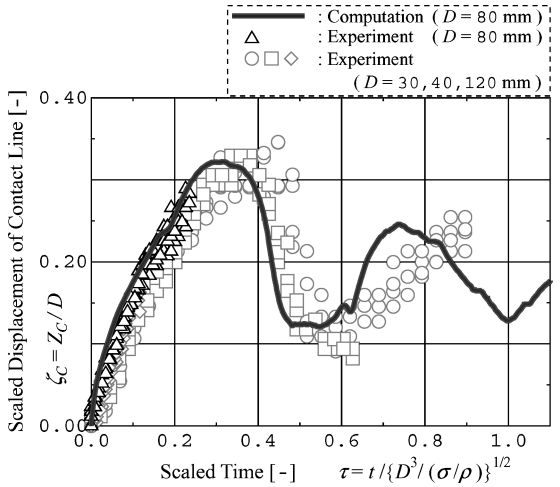

Fig. 15 Scaled displacement of the contact line, ζ_{CP}, as a function of the scaled time τ (ethanol, computed results with the boundary condition of viscous wall).

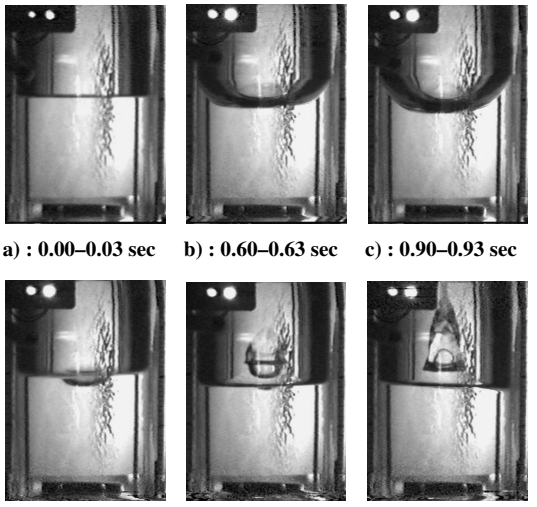

a) : 0.00–0.03 sec **b) : 0.60–0.63 sec** **c) : 0.90–0.93 sec**

d) : 1.00–1.03 sec **e) : 1.10–1.13 sec** **f) : 1.34–1.37 sec**

Fig. 16 Observed deformation of liquid surface in a cylindrical vessel, case 2 (ethanol and polyacrylate resin, $D = 150$ mm, experiment).

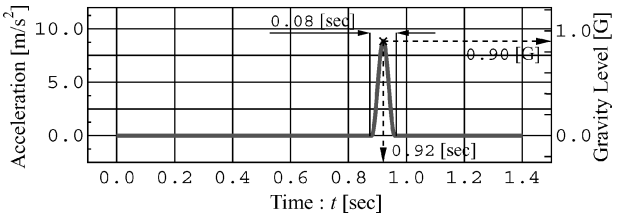

Fig. 17 History of gravity, computation.

In case 2, the diameter D and the height of the cylindrical vessel were changed to 150 and 260 mm, respectively, while the other parameters in the experiment remained unchanged. Figure 16 shows the experimental results of the surface deformation observed in the drop tower. It was observed that a liquid column was rising up and was followed by a bubble that was enclosed in it. This phenomenon was caused by the impact at about 0.9 s after the separation due to the collision between the test section and the drag shield.

In the computation for this case, the impact was taken into account although the history of the gravity during the dropping was slightly simplified as shown in Fig. 17. The symmetry with respect to the center axis was assumed and the flowfield was solved on a meridian section with 59×180 grid points allocated in the r and z directions.

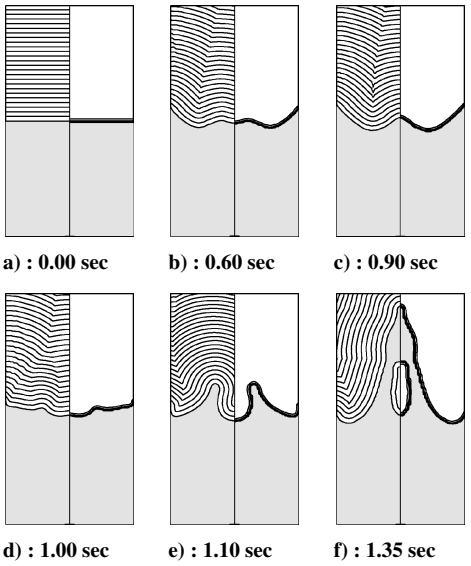

Fig. 18 Deformation of the liquid surface in a cylindrical vessel, case 2 (ethanol and polyacrylate resin, $D = 150$ mm, computation).

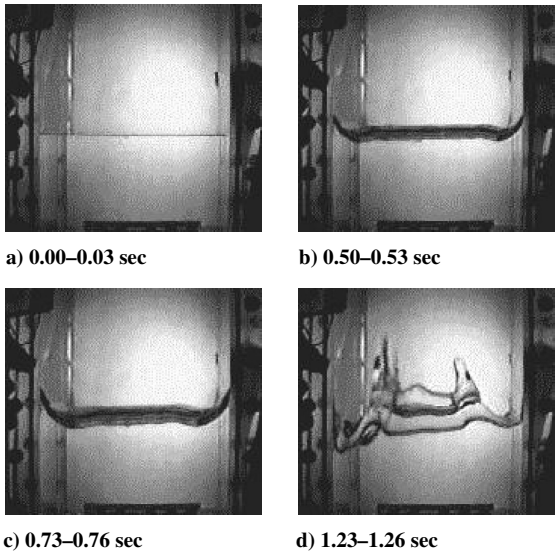

Fig. 19 Observed deformation of the liquid surface in a rectangular-shaped container, case 3 (FC-77 and polyacrylate resin, $L = 250$ mm).

Figure 18 shows the numerical results of the surface deformation in case 2, where the liquid column and the bubble caused by the collision were clearly reproduced. Hence, it can be said that the combination of the present method with the wetting model gives appropriate assessments for the behavior of free-surface flows under various gravity conditions.

Three-Dimensional Deformation

In case 3, perfluorocarbon (C_8F_{18} : FC-77) was utilized as a working fluid. To induce the three-dimensional deformation of the liquid surface, the transparent container with cylindrical shape made of polyacrylate resin was replaced by another one with rectangular shape, the dimensions of which were 150 mm in width, 145 mm in length, and 260 mm in height.

Figure 19 shows the surface deformation in case 3 observed in the drop tower. Larger deformations were observed near the corner of the vessel. To keep the advancing contact angle θ_A constant, the advancing speed of the contact points on the edge line must be faster than that on the flat wall. The liquid column caused by the collision was also observed in this case.

In the computation of case 3, the height of the container was reduced to 150 mm and $46 \times 46 \times 46$ grid points were arranged in each direction. Figure 20 shows the numerical results, where the configuration of the interface was represented by the contour surface of the zero level set ($\phi = 0$) and visualized from the viewpoint corresponding to the experimental data. Figures 21a and 21b indicate the same result as in Figures 20c and 20d, respectively, from another viewpoint. The corner effect on the wetting phenomena was reproduced in the three-dimensional computation and the calculated configuration of the interface shows good agreement with the experimental data.

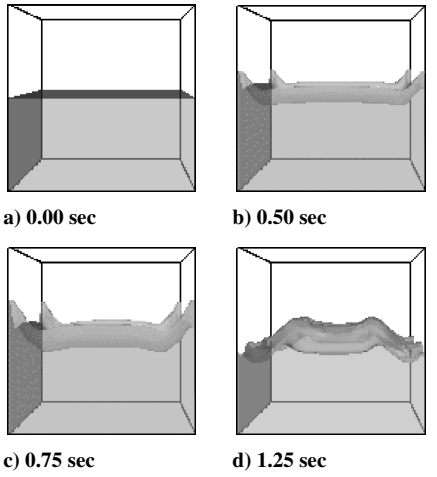

Fig. 20 Deformation of the liquid surface in a rectangular-shaped container, case 3 (FC-77 and polyacrylate resin, $L = 250$ mm, computation).

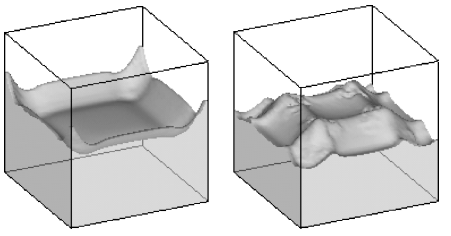

Fig. 21 Figures 20c and 20d from another viewpoint.

Hence, it was possible to say that the free-surface flows driven by surface tension, wetting phenomena, and gravity force were adequately simulated by CIP-LSM and that the algorithm and the wetting model proposed here were applicable to three-dimensional problems.

Problems in Propellant Tanks

The second-stage propulsion system of the H-IIA launch vehicle acquires multiple-ignition capability by the LE-5B engine. At the last ignition, it is important to precisely determine the serviceable amount of residual propellant.[19] In this study, to obtain the basic knowledge of the estimation of the amount, the flowfields in the propellant tank were numerically investigated under low-gravity conditions with the developed code.

Tank in Computation

Figure 22 shows the configuration of the computed domain, which was similar to that of the lower bottom of the LO_X tank for the LE-5B. It has the half-ellipse cross section with diameter of 3.19×2.25 m. If we consider the cylindrical coordinates in which the z axis is aligned in the central axis of the tank, its elliptical shape can be described as

$$\frac{r^2}{(3.19/2)^2} + \frac{(z - 2.25/2)^2}{(2.25/2)^2} = 1 \tag{46}$$

To prevent the gas suction directly into the feed line, a circular cover plate was put over the outlet. For the numerical analysis, the detailed

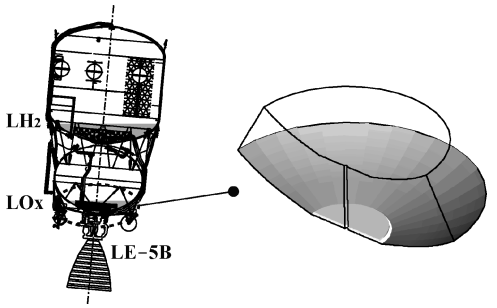

a) Configuration of Tank

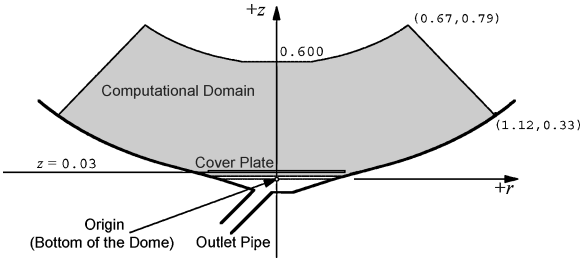

b) Computational Domain

Fig. 22 Computational domain for LO_X tank H-IIA, upper stage.

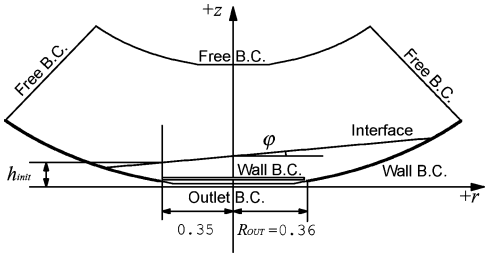

Fig. 23 Surface configuration at the initial state determined by φ and h_{init}.

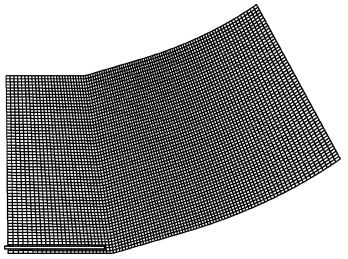

Fig. 24 Grid system for the LO_X tank (101×61 grid points in a meridian section).

geometry of the tank was slightly simplified; namely, antivortex baffles on the cover were removed.

In the upper stage of H-IIA, propellants are retained on the bottom of the tank during the coasting by a thruster of the reaction control subsystem. As shown in Fig. 23, the configuration of the interface at the initial state was given as a plane inclined by φ deg, because the direction of the retention thrust could be at an angle of 5 deg to the roll axis of the vehicle. The level of the interface was determined by initial height h_{init} defined as the lowest height of the inclined surface measured from the outer edge of the cover plate. In this domain, 101×61 grid points were allocated on the meridian section as shown in Fig. 24, and 18 grid points in the circumferential direction.

Computational Conditions

In the first case, the initial height and the inclination were set to be 159 mm and 5 deg, respectively, and the gravity remained zero. The operating fluids in this case were LO_X and GO_X. Both phases were supposed to be incompressible and their physical properties were given at the initial temperature of 90 K and pressure of 2.3×10^5 Pa.

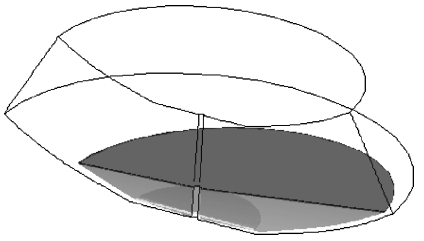

a) Initial condition : $t = 0.00$ sec

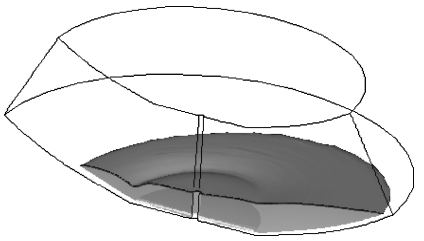

b) Growing dip : $t = 2.00$ sec

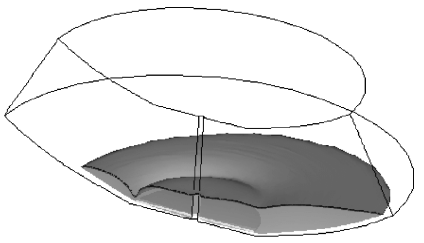

c) Gas suction : $t = 3.15$ sec

Fig. 25 Surface variation with time ($\varphi = 5$ deg, $h_{\text{init}} = 159$ mm, gravity $= 0.0000g$).

On the outlet boundary under the cover plate, the velocity profile in the z direction, w_{OUT}, was specified as

$$w_{\text{OUT}} = -(\dot{Q}/2\pi R_{\text{OUT}}) \cdot 1/r \tag{47}$$

where the drain rate was denoted by $\dot{Q}$ and fixed to be 13.6×10^{-3} m^3/s, which was 60% of the flow rate of the nominal rate. On the wall and the cover plate, nonslip conditions were imposed.

Deformation of Interface

The numerical results of the surface deformation with time are visualized in Fig. 25. In the draining process, it was found that the liquid surface was sinking over the outer edge of the cover plate just after the start of suction (see Fig. 25a). Since the steep gradient of pressure near the outlet accelerated the fluids, the dip easily penetrated into the liquid phase toward the port, and the gas suction eventually took place, as shown in Fig. 25c. It was seen that the gas was sucked at the position where the surface had been closest to the edge at the initial state.

Gas Suction Time

Figure 26 shows the time of gas suction, t_S, measured from the start of draining against initial height h_{init}. For the result indicated by the solid line, the initial inclination φ was set to be 5 deg; the result with no inclination is represented by broken lines. In these cases, the draining rate was fixed to be 60% of the nominal flow rate. Despite the difference in inclination, the two series of the results nearly correspond to each other. This means that the gas suction time should have a good correlation with the initial interface height as long as the inclination of the interface is relatively small.

In Fig. 27, the gas suction time is shown as a function of the initial interface height at various draining rates under zero- and low-gravity conditions. The broken lines represent numerical results in a weightless state and the solid lines represent those under the low-gravity condition of $0.0006g$. The flow rate ranged from 24 to 60% of the nominal flow rate. For the results of zero gravity, the gas

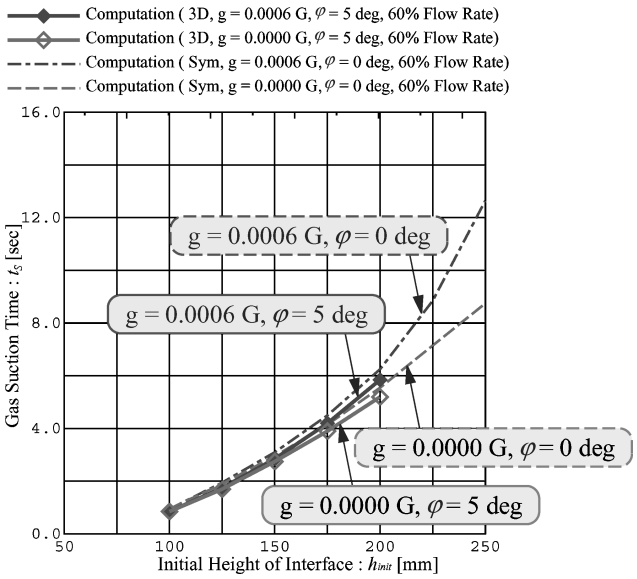

Fig. 26 Gas suction time as a function of initial height at fixed drain rate: comparison of the three-dimensional results with the axisymmetric results.

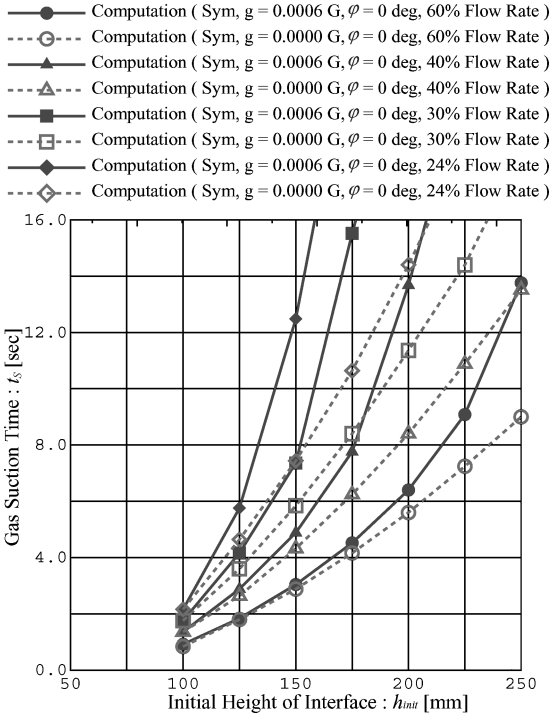

Fig. 27 Effect of acceleration on the gas suction time at various draining rates.

suction time is inversely proportional to the flow rate. In the results with acceleration, the estimated values of the gas suction time are almost identical to those in a weightless state for the small initial height. On the other hand, the time considerably delays when the height is increased. It is therefore realized that the buoyancy induced by a slight acceleration of $0.0006g$ should not be neglected in the simulation of draining problems in the tanks of launch vehicles.

In the reignition process of LE-5B, the acceleration as much as $2g$ is thought to be large enough to suppress the growth of the dip on the surface of the liquid propellant. In addition, the gas suction time was also affected by the acceleration history and the occurrence of sloshing.

The numerical analysis under realistic conditions is expected to estimate the serviceable amount of the residual propellant precisely.

Conclusions

In the present study, to capture the three-dimensional deformation of a liquid surface in storage tanks on orbit, a numerical method called CIP-LSM was developed. In this method, the algorithm of the CCUP scheme and LSM was modified and extended to the generalized curved linear coordinate in a three-dimensional domain. On the basis of the CSF model, both surface tension and wetting phenomena were introduced as body forces. The numerical results calculated with the developed code were compared with the corresponding experimental data obtained in the drop test, and good agreement was obtained between them. The conclusions are as follows:

1) The algorithm of the CIP scheme is applicable to the reinitialization of the level set function.

2) The wetting model based on the CSF model was applicable to three-dimensional problems. It is important to consider the advancing and receding contact angle for the quantitative prediction of unsteady change caused by wetting phenomena.

To accumulate the basic knowledge about the unsteady changes of free-surface flows driven by surface tension, the deformation of a gas–liquid interface in a cylindrical or a rectangular-shaped vessel was visualized under low-gravity conditions obtained with a drop tower. The conclusions are summarized as follows:

3) In the cylinder, the scaled displacement of the contact line, ζ_{CP}, on the solid wall has a good correlation with the scaled time τ and the contact angle. The similarity law works as long as the viscosity is negligible in the flowfield.

For the estimation of the serviceable amount of the small residual propellant at reignition process, the flowfields in the LO_X for the LE-5B engine under low-gravity conditions were numerically investigated. In the results, the generation of the dip was clearly shown, and the phenomenon of gas suction was properly reproduced. The conclusions obtained from the calculations are as follows:

4) As long as the inclination of the liquid surface φ is small, under 5 deg, the gas suction time t_S has a good correlation with the initial interface height h_{init}.

5) The buoyancy induced by a slight acceleration of as much as $10^{-3}g$ is effective to prevent the dip growth and to increase the serviceable propellant of launch vehicles.

The developed analysis method is expected to clarify the various aspects of gas–liquid two-phase flow behavior in the field of space applications.

Acknowledgments

Financial support by the Japan Society for the Promotion of Science, Grant No. 12-09317, is gratefully acknowledged. The present experiments were conducted through the collaboration with K. Hayashi, S. Muramatsu, T. Fujiwara, Y. Kano, and K. Okai with the help of M. Kono and M. Tsue, who provided the experimental opportunity in the drop tower at the University of Tokyo. A lot of valuable discussions for the numerical analysis were held with M. Tsuboi and M. Fukuzoe of the Japan Aerospace Exploration Agency. The authors give great thanks to them.

References

[1]Reynolds, W. C., and Statterlee, H. M., "Liquid Propellant Behavior at Low and Zero g," *The Dynamic Behavior of Liquids in Moving Containers*, edited by H. N. Abramson, NASA SP-106, Washington, D.C., 1966, pp. 387–449.

[2]Antar, B. N., and Nuotio-Antar, V. S., *Fundamentals of Low Gravity Fluid Dynamics and Heat Transfer*, CRC Press, Boca Raton, FL, 1993.

[3]Himeno, T., Watanabe, T., and Konno, A., "Numerical Analysis of Two-Phase Flow Behavior in a Liquid Propellant Tank," AIAA Paper 99-2177, July 1999.

[4]Himeno, T., and Watanabe, T., "Thermo-Fluid Management Under Low-Gravity Conditions: 2nd Report, Free-Surface Flows Driven by Surface Forces," *Transaction of the Japan Society of Mechanical Engineers, Series B*, Vol. 68, No. 687, 2003, pp. 2400–2407.

[5]Himeno, T., "Thermo-Fluid Behavior of Two Phase Flow Under Low-Gravity Condition," Ph.D. Dissertation, Dept. of Aeronautics and Astronautics, Univ. of Tokyo, Tokyo, 2001.

[6]Gerstmann, J., Michaelis, M., Drayer, M., and Rath, H. J., "An Applicable Boundary Condition at the Moving Contact Line in Case of a Free Surface

Reorientation After Step Reduction in Gravity," Proceedings in Applied Mathematics and Mechanics, No. 2, March 2003, pp. 316, 317.

[7]Michaelis, M., "Kapillarinduzierte Schwingungen freier Flussigkeitsoberflachen," Ph.D. Dissertation, Universitat Bremen, VDI Verlag, Dusseldorf, Germany, 2003.

[8]Yabe, T., and Wang, P. Y., "Unified Numerical Procedure for Compressible and Incompressible Fluid," *Journal of the Physical Society of Japan*, Vol. 60, No. 7, 1991, pp. 2105–2108.

[9]Sussman, M., Smereka, P., and Osher, S., "A Level Set Approach for Computing Solutions to Incompressible Two-Phase Flow," *Journal of Computational Physics*, Vol. 114, 1994, pp. 146–159.

[10]Osher, S., and Sethian, J. A., "Front Propagating with Curvature-Depending Speed: Algorithms Based on Hamilton-Jacobi Formulations," *Journal of Computational Physics*, Vol. 79, 1988, pp. 12–49.

[11]Brackbill, J. U., Kothe, D. B., and Zemach, C., "A Continuum Method for Modeling Surface Tension," *Journal of Computational Physics*, Vol. 100, 1992, pp. 335–354.

[12]Yabe, T., and Takei, E., "A New Higher-Order Godnov Method for General Hyperbolic Equations," *Journal of the Physical Society of Japan*, Vol. 57, No. 8, 1988, pp. 2598–2601.

[13]Yabe, T., Xiao, F., and Utsumi, T., "The Constrained Interpolation Profile Method for Multiphase Analysis," *Journal of Computational Physics*, Vol. 169, No. 2, 2001, pp. 556–593.

[14]Himeno, T., Nonaka, S., Naruo, Y., Inatani, Y., and Watanabe, T., "Prediction of Sloshing in the Propellant Tank of Reusable Rocket Vehicle," AIAA Paper 2003-4894, July 2003.

[15]Kunugi, T., Satake, S., and Ose, Y., *International Journal of Heat and Fluid Flow*, Vol. 22, No. 3, 2001, pp. 245–251.

[16]Kunugi, T., "MARS for Multiphase Calculation," *Computational Fluid Dynamics Journal*, Vol. 9, No. 1, 2000, pp. 563–571.

[17]Hirt, C. W., and Nichols, B. D., "Volume of Fluid (VOF) Method for the Dynamics of Free Boundaries," *Journal of Computational Physics*, Vol. 39, 1981, p. 201–225.

[18]Youngs, D. L., "Time-Dependent Multi-Material Flow with Large Fluid Distortion," *Numerical Methods for Fluids Dynamics*, edited by K. W. Morton and M. J. Baines, Academic Press, Massachusetts, 1982.

[19]Nagoya Aerospace System Works, Mitsubishi Heavy Industries, "Study on Multiple Ignition Technology for H-IIA Upper Stage," NASDA NU-90341, National Space Development Agency of Japan, Tokyo, 1996, Chap. 4.2.2.